

Supporting information

Physiological Sensing System Integrated with Vibration Sensor and Frequency Gel Dampers Inspired by Spider

Jianren Huang,^a Anbang Chen,^a Jinrong Liao,^b Songjiu Han,^a Qirui Wu,^a Jiayu Zhang,^a

Yujia Chen,^a Xiandong Lin,^b Lunhui Guan^{a,}*

^aCAS Key Laboratory of Design and Assembly of Functional Nanostructures,
Fujian Key Laboratory of Nanomaterials, Fujian Institute of Research on the Structure
of Matter, Chinese Academy of Sciences, Fuzhou 350108, China.

^bLaboratory of Radiation Oncology and Radiobiology, Fujian Medical University Cancer
Hospital, Fujian Cancer Hospital, Fuzhou 350014, China

E-mail: guanlh@fjirsm.ac.cn (L.Guan)

Supplementary Note 1. Material and fabrication

Fabrication of Electrospinning TPU Substrate: Dissolved TPU pellets in a tetrahydrofuran(TMf)/dimethyl formamide(DMF) solution with a concentration of 15 wt%. The homogeneous polymer precursor was loaded into a syringe. The electrospinning was applied to a feeding rate with the volumetric flow at 2.0 mL h⁻¹. The charged jet of polymer solution solidified into ultrafine fibers as it traveled towards the collector. The fibers were collected on the collector in the form of a network structure. After the electrospinning process was complete, The TPU substrate can be further processed by surface treatment with plasma.

Synthesis of conductive MXene Flake: 1.6 g of lithium fluoride (LiF) was added to 20 ml of hydrochloric acid (HCl) with a concentration of 9 M to create the HF etching solution. The solution was thoroughly mixed using magnetic stirring. Then, 1 g of the Ti₃AlC₂ MAX phase flakes was slowly added to the etching solution. The reaction was allowed to proceed at a temperature of 45°C for a duration of 24 hours. Following the etching process, the resulting product was subjected to multiple washes with deionized water. The mixture was then centrifuged at 3500 rpm for 10 minutes until the supernatant reached a pH value of approximately 6-7. To further process the MXene flakes, the MXene solution was frozen and placed in a freeze dryer. The freeze-drying process facilitated the sublimation of ice, resulting in the formation of MXene solid powder.

Preparation of PDMS elastomer: Mix the PDMS base and curing agent in the desired ratio (typically 1:10), stir thoroughly, and then degas the mixture under vacuum to remove bubbles. Afterward, pour the mixture into molds or onto the desired surface and cure it at 80 °C for 2 h, depending on the desired hardness and thickness. Finally, demold the PDMS once it's fully cured.

Fabrication of damper integrated vibration sensor: The crack sensor and data acquisition system were connected by a conductive silver wire. A piece of damper gel with a 10 mm × 5mm × 2 mm thickness were gently placed on the sensors. Meanwhile, commercial PDMS server as reference.

Supplementary Note 1. Characterizations and Measurements

Material Characterizations: In the characterization of the gel damper and TPU@MXene crack sensor, the Field-Emission Scanning Electron Microscopy (Verios G4, America) instrument was operated at an acceleration voltage of 5 kV. Thermogravimetric analysis (TGA) was performed using a TG-DTA instrument (STA449F5) between 25 to 800 °C at a heating speed of 10 °C min⁻¹

under an argon atmosphere. XPS measurements were performed using an ESCALAB 250Xi instrument. X-ray diffraction (XRD) spectra were obtained within a 2θ range of 5 to 70 degrees using a MiniFlex-II diffractometer manufactured by Rigaku in Japan. The water contact angles were measured by POWEREACH JC200D1 goniometer.

Tensile Testing: The TPU hybrid gel was cut into dumbbell-shaped specimens with a gauge width of 3 mm for uniaxial stretching tests. The thickness of the sample was quantitated with a caliper and was approximately 0.15 mm. The stress-strain curves were acquired using a universal material test machine (AG-X plus, SHIMADZU, Japan) equipped with 100 N loading cells.

Measurement of the interfacial toughness: The interfacial toughness of the crack sensor adhered on a gel damper was measured using the standard 90°-peeling test with a mechanical testing machine (AG-X plus, SHIMADZU). One end of a sample is bonded to a substrate, and the other end is pulled at a constant rate. The energy required to peel the interface is then calculated, which represents the interfacial toughness. All tests were performed either in ambient air at room temperature.

Cell biocompatibility in vitro: Human umbilical vein endothelial cells (HUVECs) (Kebai Biotech Co. Ltd, Nanjing, China) were sterilized under high temperature and pressure. HUVECs were suspended in the medium, and the HUVEC density was calculated as 4×10^5 cells mL⁻¹ using a hemocytometer. The HUVECs were inoculated on a hybrid film with a density of 2×10^4 cells in the pores of the tissue culture plate and stored in a medium supplemented with BEGM Bronchial Epithelial Cell Growth Medium BulletKit (Lonza) at 37 °C in an incubator with 5% CO₂. The cells (HUVECs) were cultured in vitro for 24 (1 day), 72 (3 days) and 168 h (7 days), stained with 250 μL Calcein AM/PI for 30 min, and then washed three times with phosphate-buffered saline (PBS). The cultured and stained HUVECs were placed on film and observed under fluorescence microscope (Leica DMI8, Germany). Data are represented as mean±S.D. examined over three independent experiments.

Cells proliferation assay: After adding 10 μL of CCK8 (Dojindo, Japan) and 90 μL RPMI 1640 medium into each plate of cells, the sections were incubated at 37°C under 5% CO₂, and microplate reader (Biotek) was subsequently used to measure OD value. The proliferative-detection was performed at 24, 48, and 72 hours after HUVECs inoculated on samples. Analyze the OD values obtained at different time points to assess the proliferative activity of the HUVECs on the samples.

Supplementary figures and tables

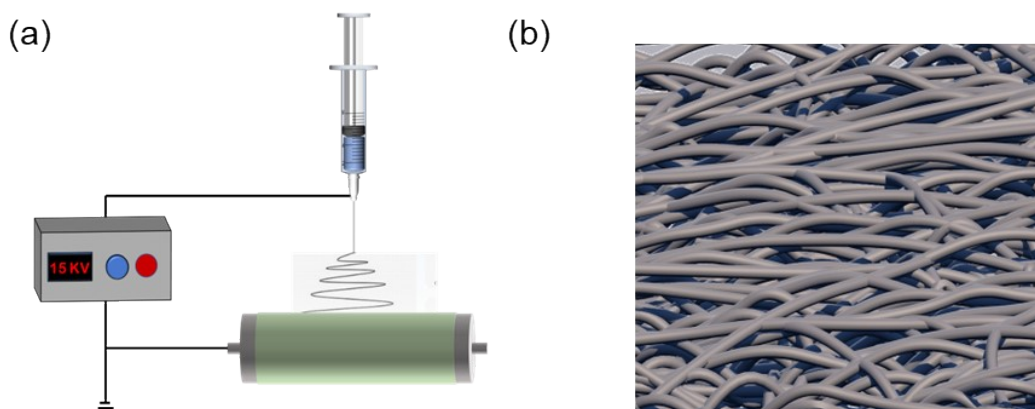


Figure S1. TPU fiber manufacturing based on Electrospinning

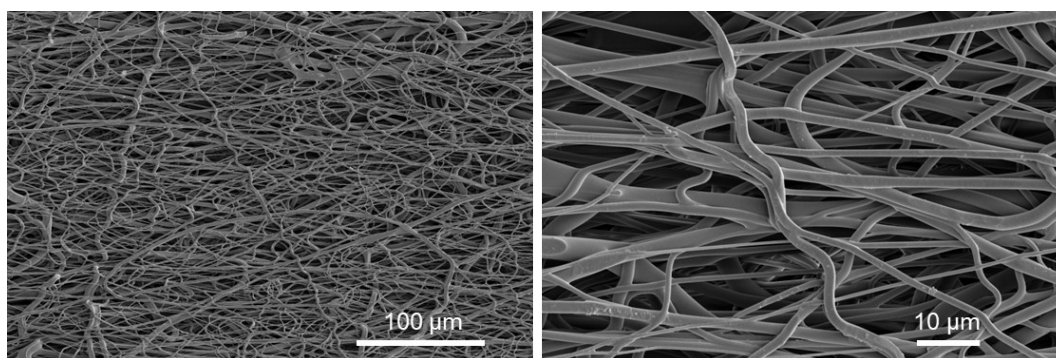


Figure S2. *In-suit* SEM image of pure electrospun TPU fiber network under a strain of 50% (in horizontal direction).

Electrospinning can produce ultrafine fibers with diameters in the nanometer to micrometer range. The small fiber diameter enhances the mechanical properties, such as tensile strength and flexibility. This flexibility makes them suitable for use in flexible electronics and wearable devices.

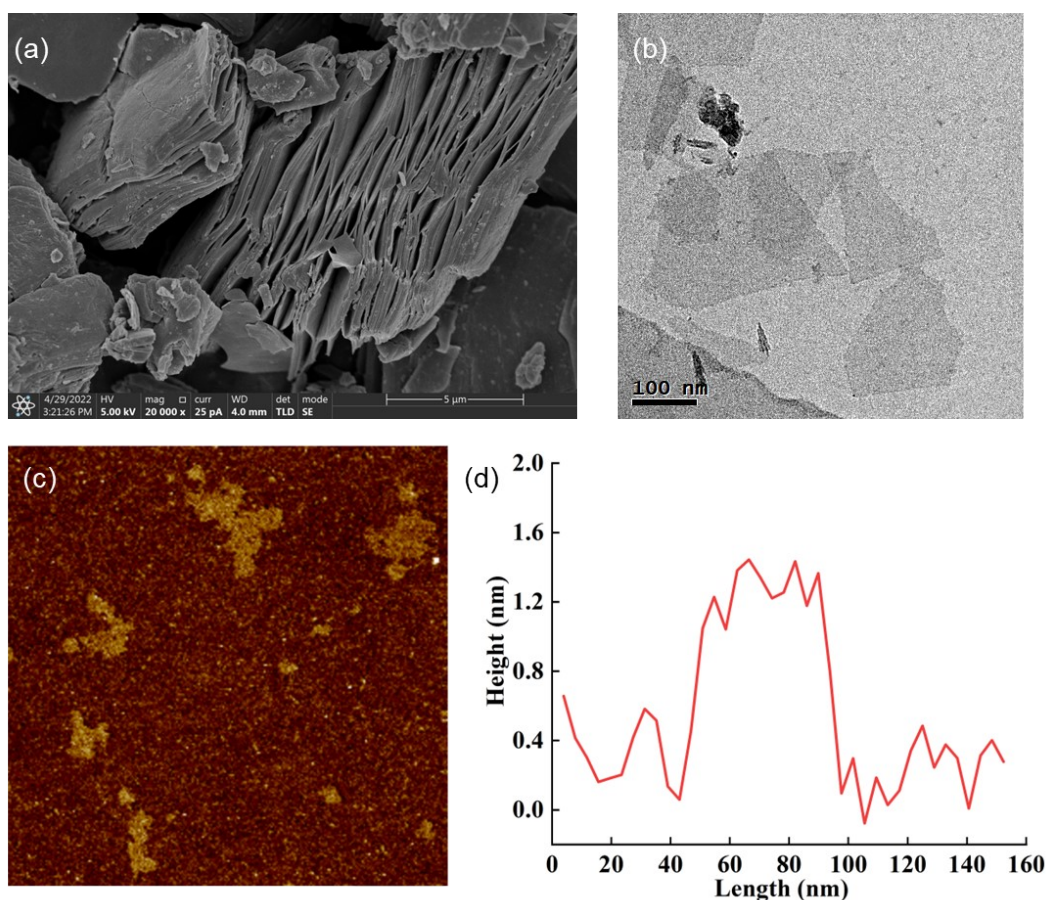


Figure S3. the synthesized of $\text{Ti}_3\text{C}_2\text{T}_x$ materials. (a) SEM image of the multi-layer $\text{Ti}_3\text{C}_2\text{T}_x$ MXene. (b) TEM image of the sonicated monolayer $\text{Ti}_3\text{C}_2\text{T}_x$ MXene with small size. (c) and (d) The AFM image and corresponding height profile of $\text{Ti}_3\text{C}_2\text{T}_x$ MXene flakes.

The MAX phase Ti_3AlC_2 was subjected to a selective etching process, during which the A element (Al) was removed from the crystal structure. This process resulted in the transformation of Ti_3AlC_2 into MXene. After the etching process, the MXene material exhibited a multilayer structure that was loosely stacked, resembling an accordion-like configuration. This structure indicates that the MXene layers are not strongly bound to each other, and there are spaces between the layers (Figure S3a). The lateral size of the delaminated MXene nanosheets was measured to be around hundreds of nanometers (Figure S3b). This indicates that the MXene nanosheets have a size in the micrometer range, making them suitable for various applications that require nanoscale materials. The delaminated MXene nanosheets, which were obtained after exfoliating the material, have an ultrathin structure with a thickness of approximately 2 nanometers (Figure S3c and 1d). This suggests that the individual MXene layers are very thin, contributing to the 2D nature of MXene

materials. The combination of an accordion-like multilayer structure and ultrathin nanosheet morphology is characteristic of MXene materials and contributes to their unique properties, such as high electrical conductivity and surface functionality.

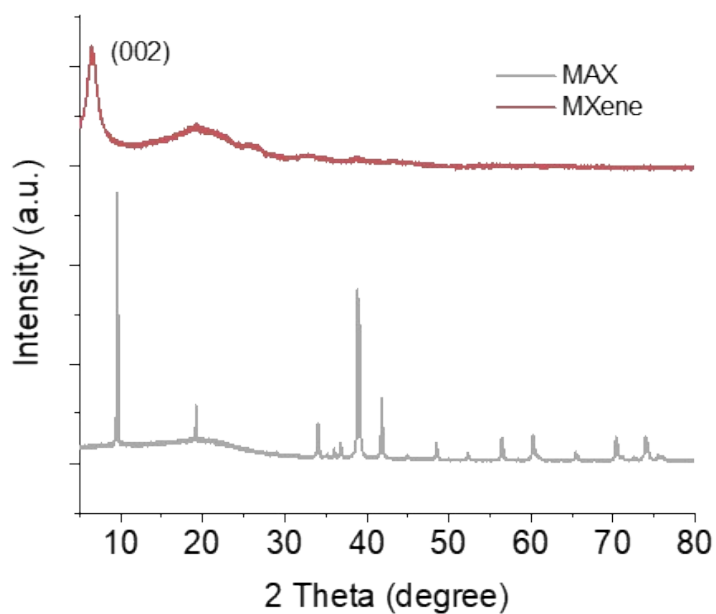


Figure S4. XRD patterns of MAX phase (Ti_3AlC_2) and $\text{Ti}_3\text{C}_2\text{T}_x$ MXene.

X-ray diffraction (XRD) analysis: The shift of the (002) peak from 9.6° to 6.0° in the XRD pattern indicates an increase in the interlayer spacing of the MXene nanosheets compared to the MAX phase. This shift is characteristic of delamination and indicates the successful exfoliation of the layers. Besides, the disappearance of the most intense diffraction peak of Ti_3AlC_2 at 39° in the XRD pattern further confirms the selective etching of the A element (Al) from the MAX phase. This suggests that the original MAX phase has been successfully converted into MXene nanosheets.

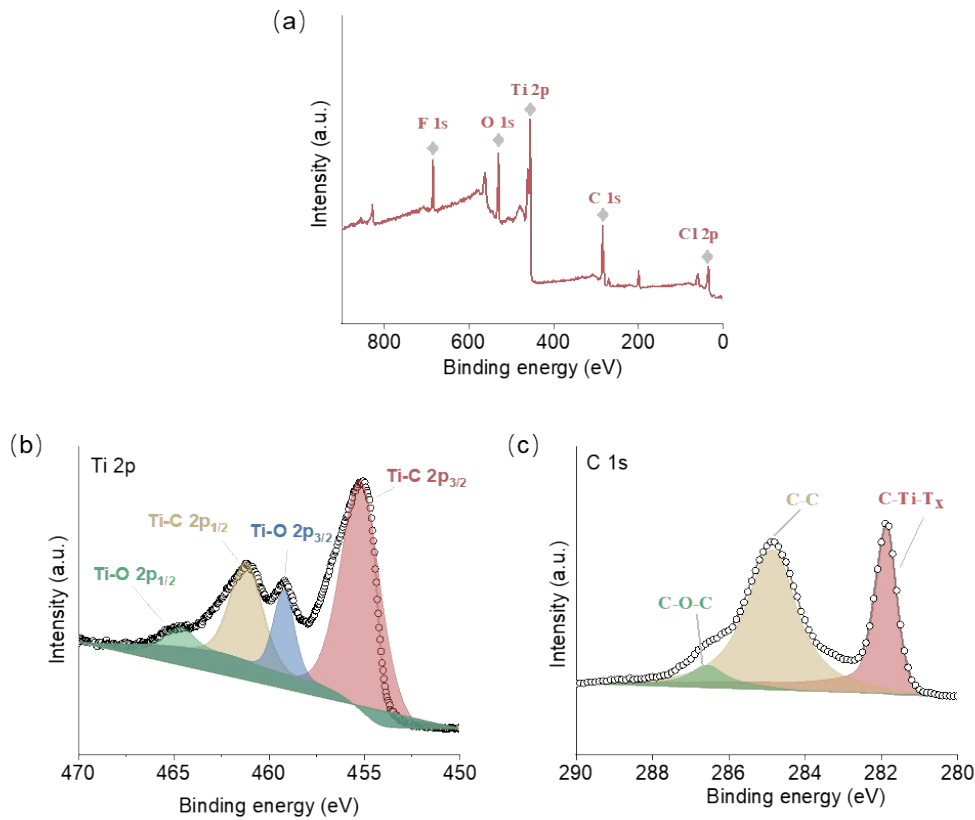


Figure S5. (a) XPS spectra of the delaminated $\text{Ti}_3\text{C}_2\text{T}_x$ MXene nanosheets. (b) Ti 2p spectra and (c) C 1s spectra of MXene.

XPS spectra were obtained for the MXene material, and the results show the presence of several elements, primarily Ti, C, O, and F. These different chemical states can provide insights into the surface chemistry and functionality of the MXene material. The Ti 2p and C 1s peak division in an XPS (X-ray Photoelectron Spectroscopy) spectrum of MXene typically reveals the chemical states and environments of titanium (Ti) and carbon (C) in the material.¹ As shown in Figure S5, The Ti 2p_{3/2} peak is the lower binding energy peak and is typically located around 454 eV. The Ti 2p_{1/2} peak is higher in binding energy, often around 460 eV.² In addition to the Ti peak, the carbon peaks also be observed in the C 1s spectrum that are associated with the various carbon species present in MXene. These carbon species may include C-C, C-O and other chemical states.³

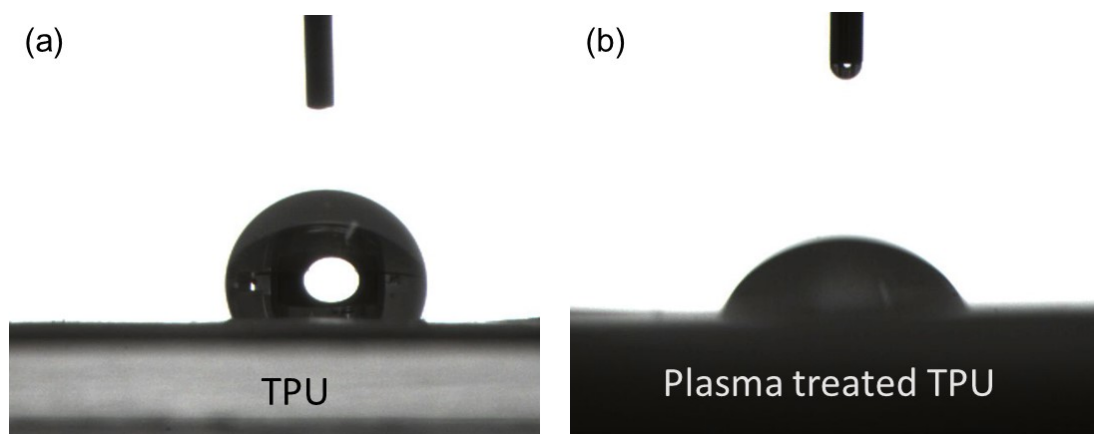
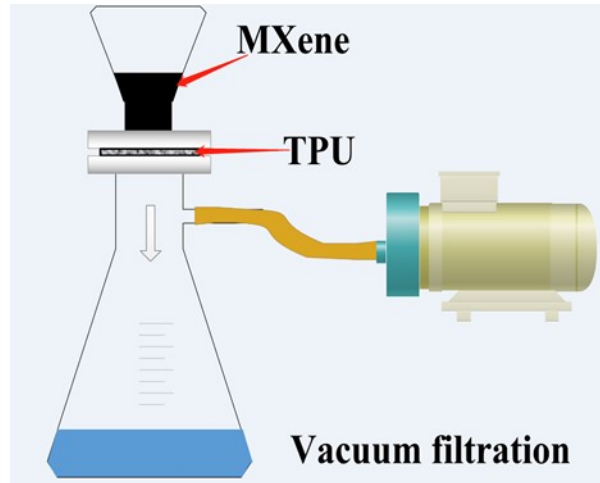


Figure S6. The photographs show the water infiltration process (a) TPU substrate and (b) oxygen plasma treated TPU film

The infiltration process was recorded of the hydrogel precursor by a CCD camera. Due to improve the hydrophilicity of the TPU substrate, allowing the water rapidly infiltrate to the whole substrate.

TPU film



Mxene@TPU film

Figure S7. The fabrication of Mxene@TPU film

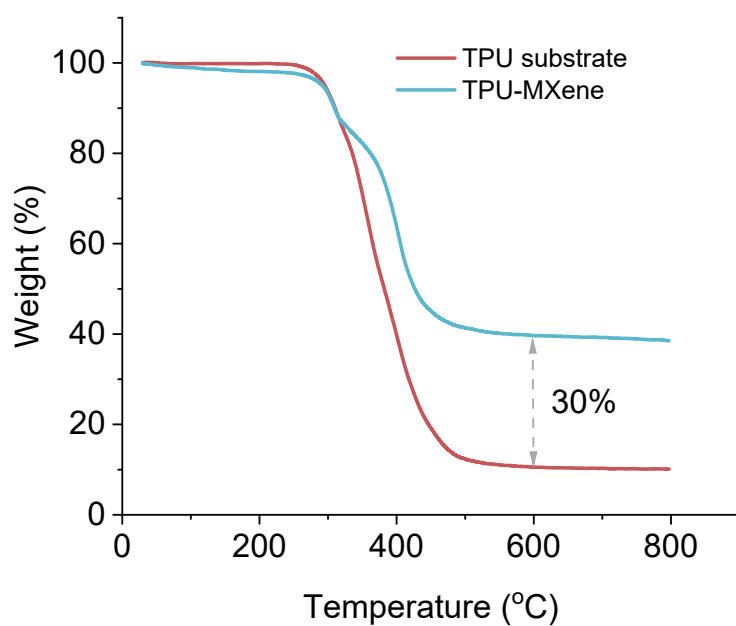


Figure S8. TGA curve of electrospinning TPU substrate and TPU@MXene film.

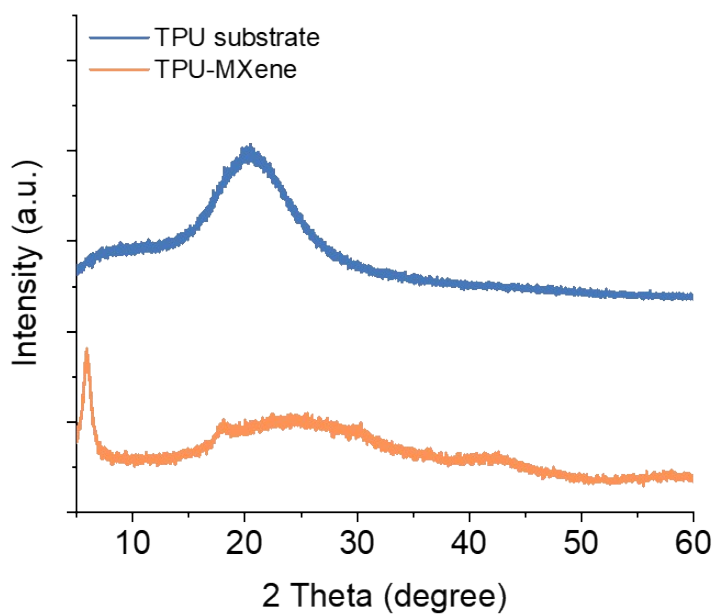


Figure S9. The XRD patterns of electrospinning TPU substrate and TPU@MXene film.

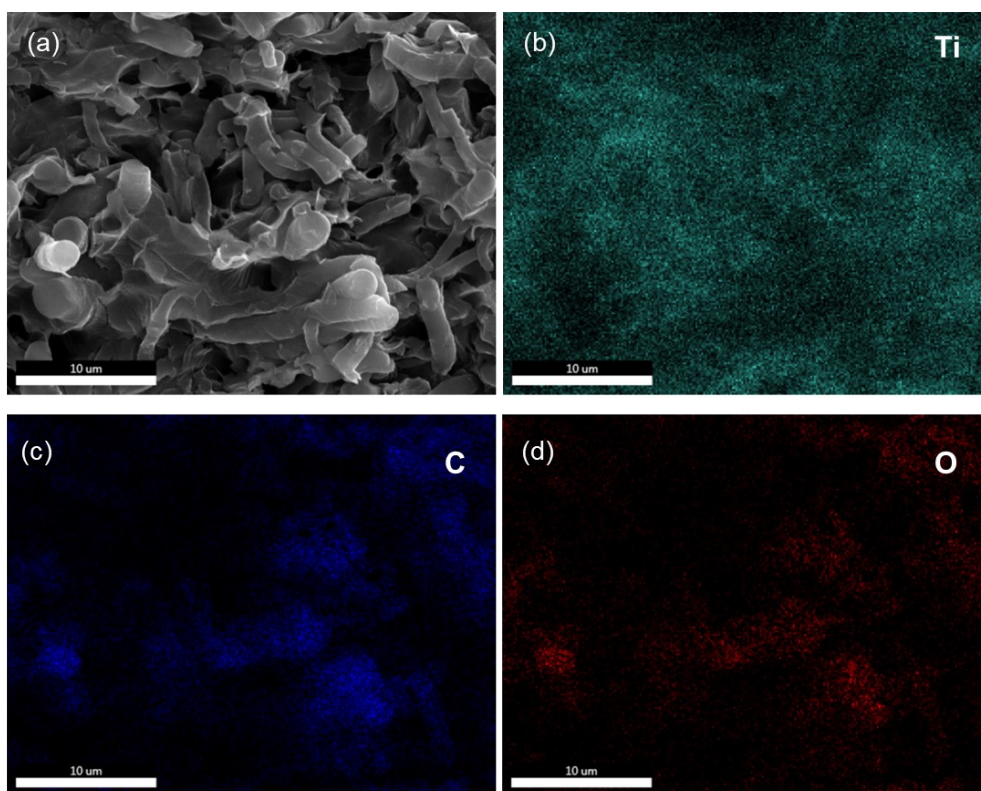


Figure S10. (a) The cross-sectional SEM image and EDS mapping of MXene@TPU film. The elements for (b) Ti, (c) C, (d) O.

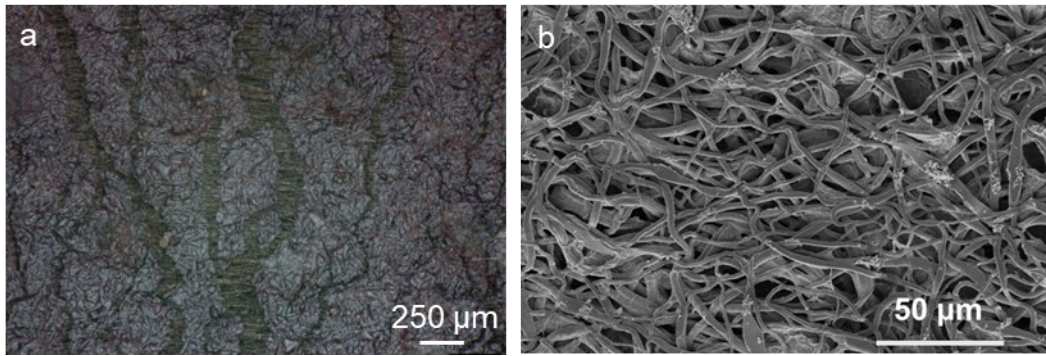


Figure S11. The surface SEM image (a) optical microscopy and (b) SEM image of prepared MXene@TPU film in surface view.

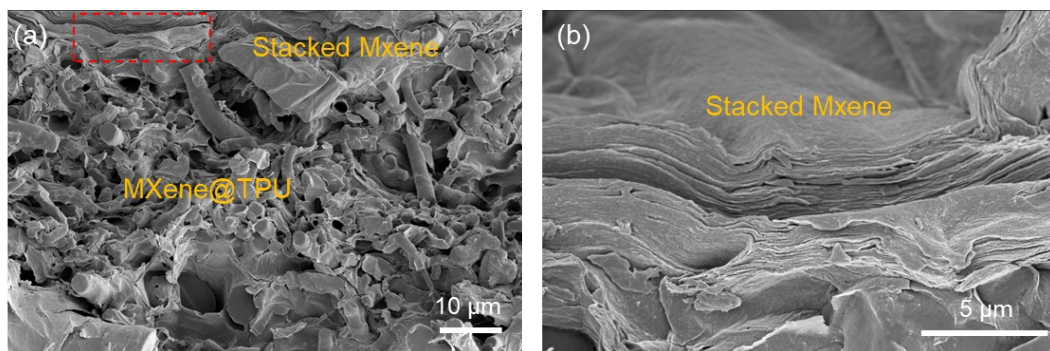
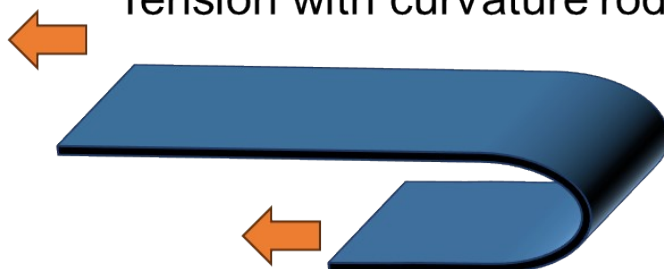


Figure S12. The Sem image illustrated excessed MXene flakes continuously accumulate on the fiber network surface.

Mxene@TPU film



Tension with curvature rod



Crack sensor

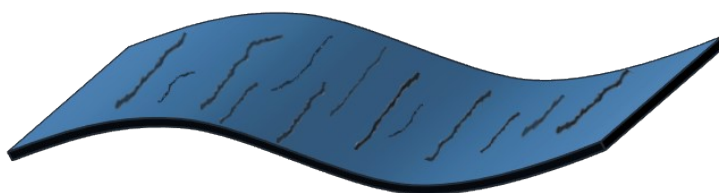


Figure S13. Schematic illustration of the process for constructing microcracks.

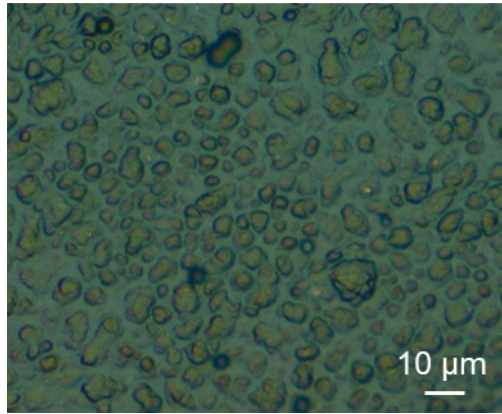


Figure S14. Optical microscopy images of gel damper in surface view.

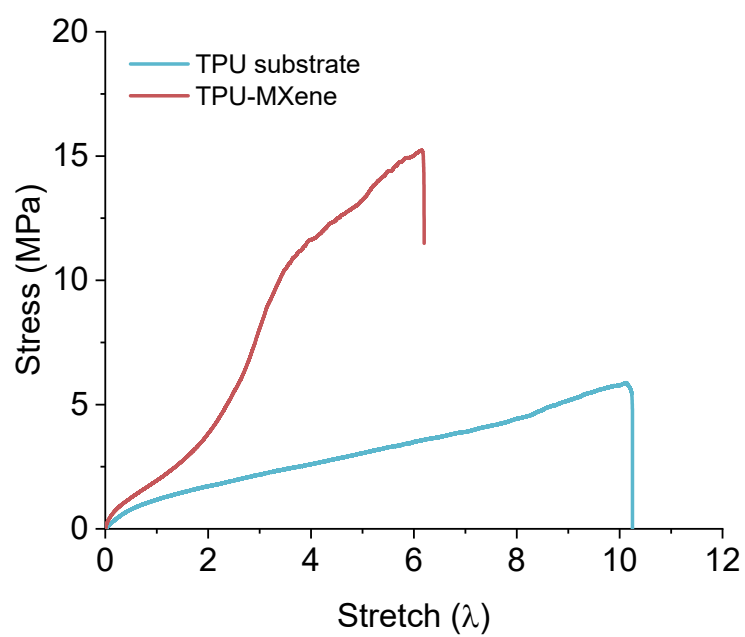


Figure S15. The typical tensile curve of the TPU substrate and TPU@MXene film.

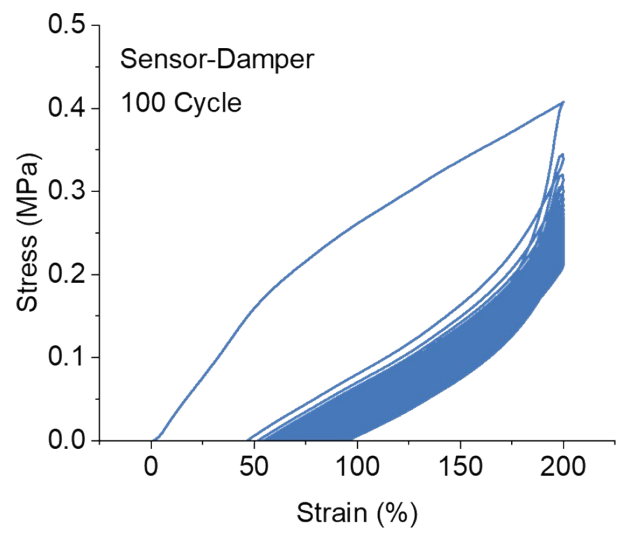


Figure S16. Cyclic stress–strain curves of sensing system at 200% strain

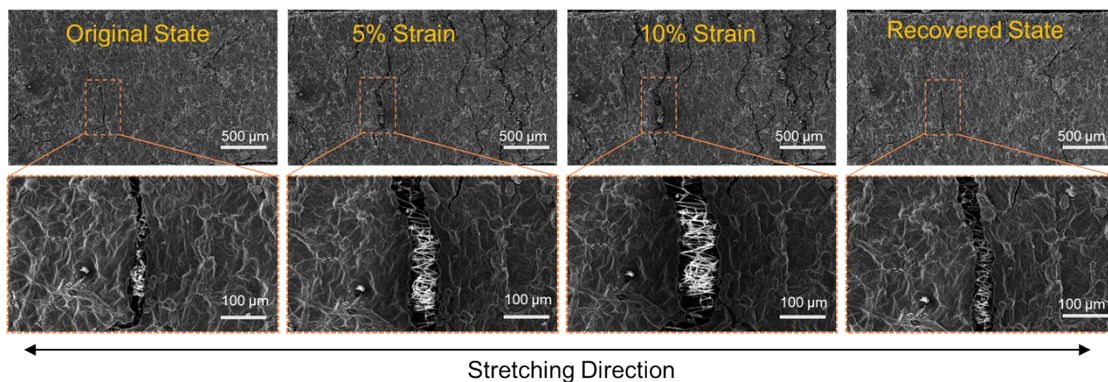


Figure S17. *In-suit* SEM image of MXene@TPU sensor during stretching and releasing process.

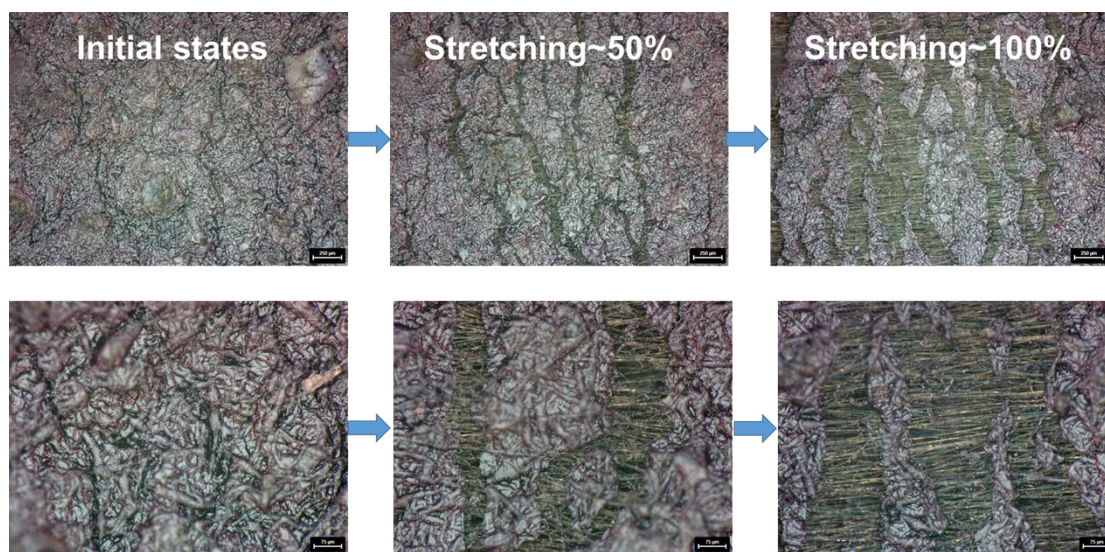


Figure S18. *In-suit* optical microscope image of MXene@TPU sensor during stretching and releasing process.

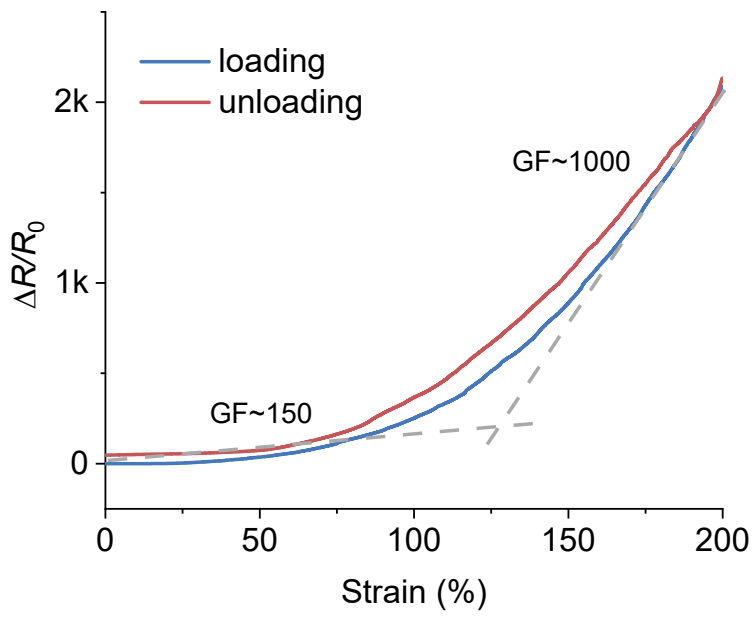


Figure S19. Relative electrical resistance–strain response curves of the crack sensor with loading and unloading process.

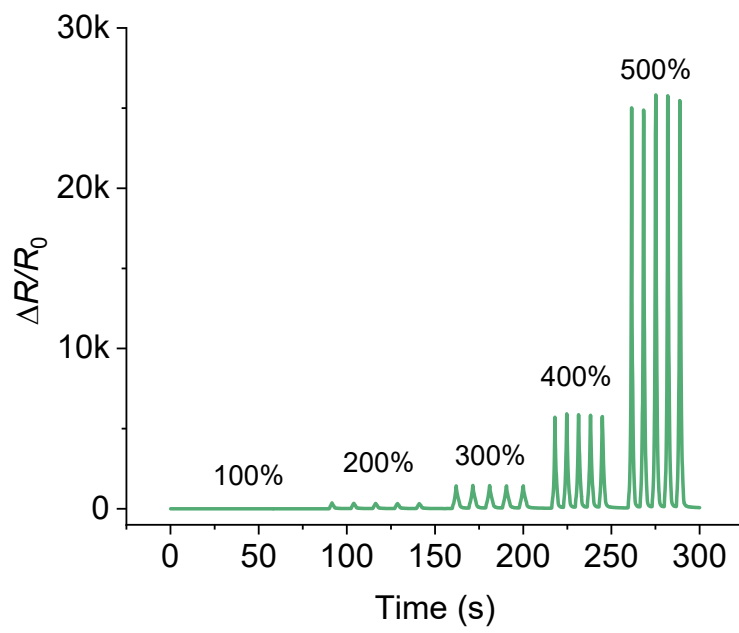


Figure S20. Cyclic tensile test responses of the crack sensor with various large strain range from 100 to 500%.

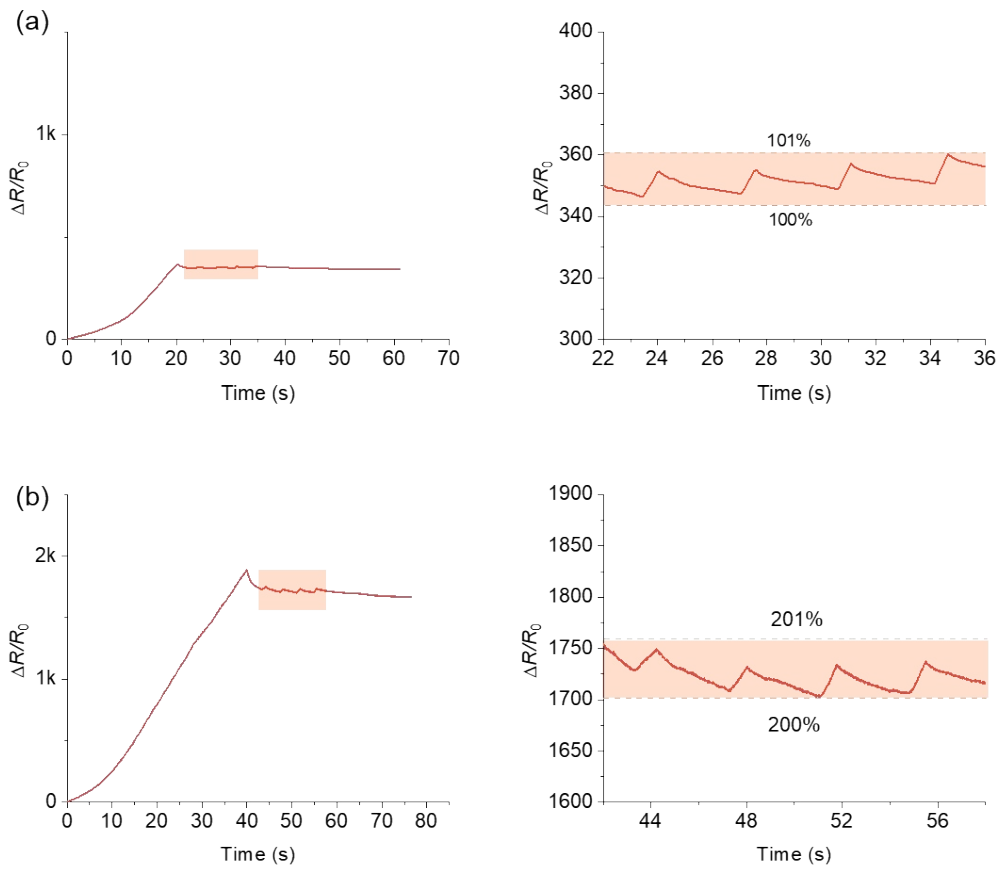


Figure S21. Detection of sequential single-step ultralow strains (1%) under a large base strain.
(a)100% and (b)200%

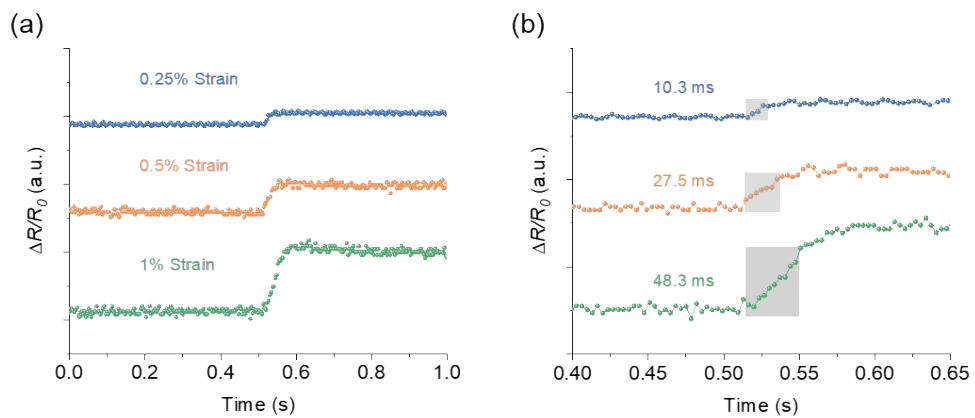


Figure S22. (a) Resistance response of the sensor under a series of tiny tensile strains of 0.25%, 0.5% and 1%. (b) corresponding response time under various loading.

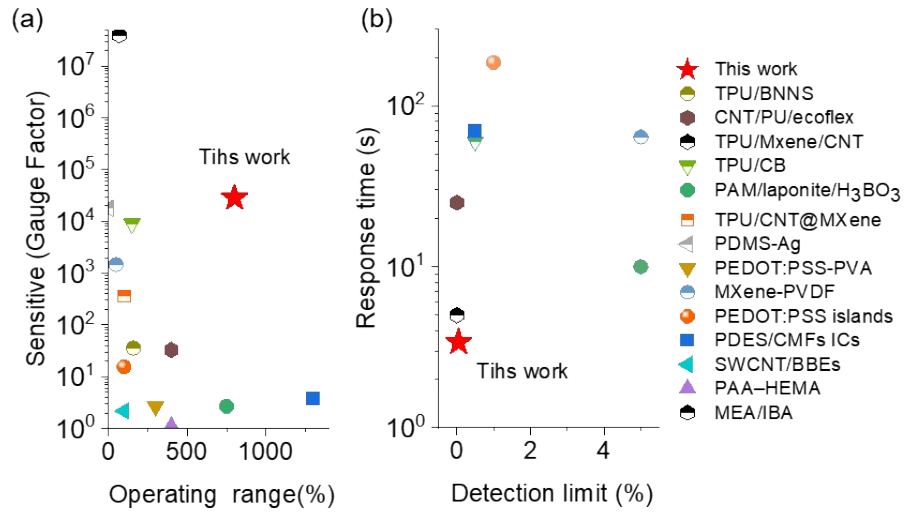


Figure S23. Ashby diagrams of (a) sensitivity versus operating range, (b) response time versus detection limit of crack sensor with other reported flexible sensor. The data used are summarized in Supporting Information of Table S1.

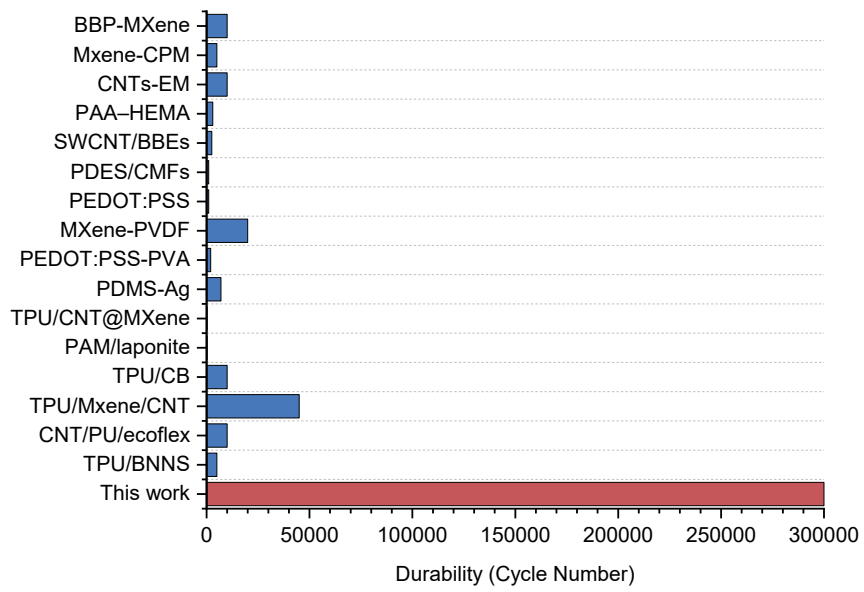


Figure S24. Cyclic performance of the crack sensor in this work compare with other reported flexible sensor. The data used are summarized in Supporting Information of Table S1.

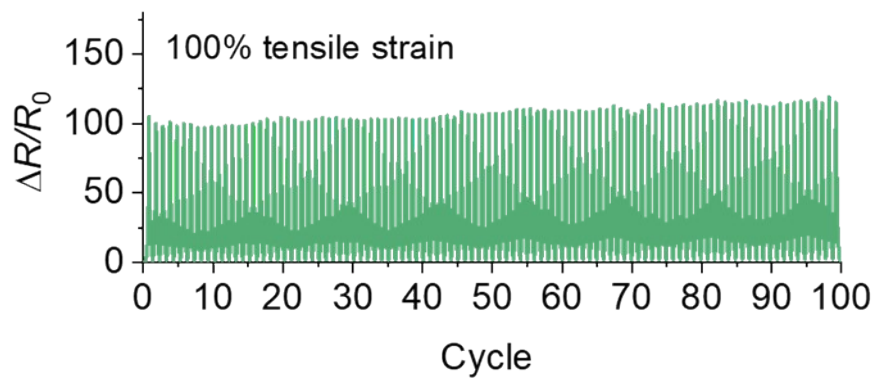
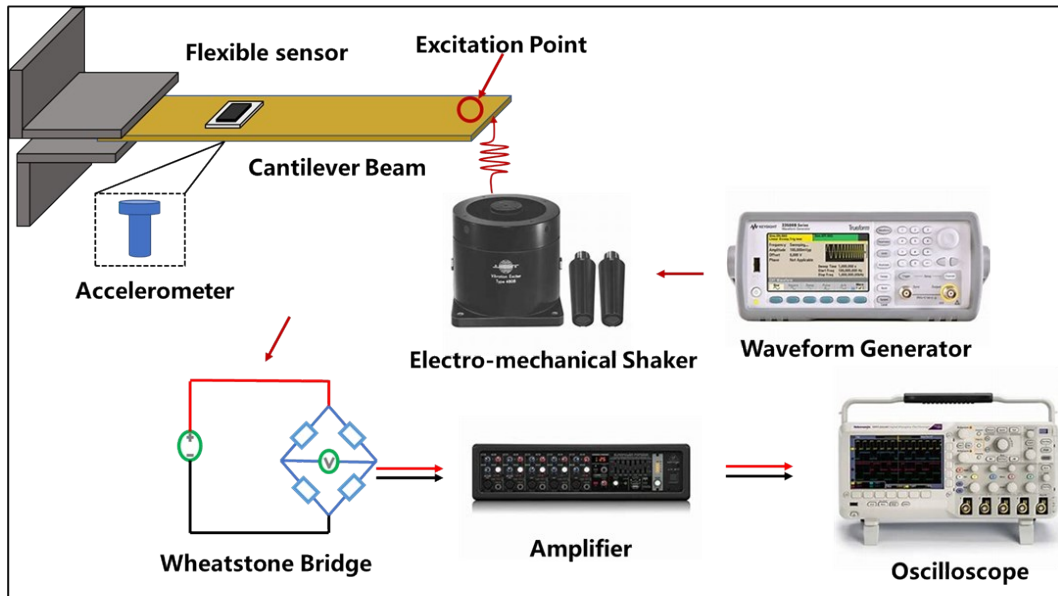


Figure S25. The relative resistance responses of the electrode during 100 stretching and releasing cycles at strain rates of 100%.

(a)



(b)

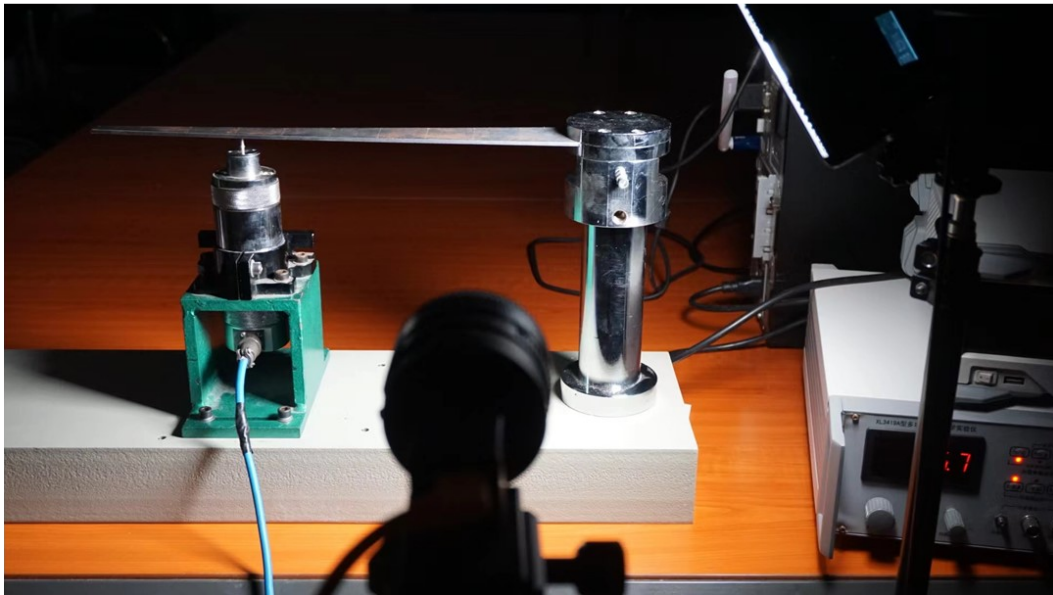


Figure S26. (a) Schematic diagram and (b) digital photos of the vibration test experimental equipment.

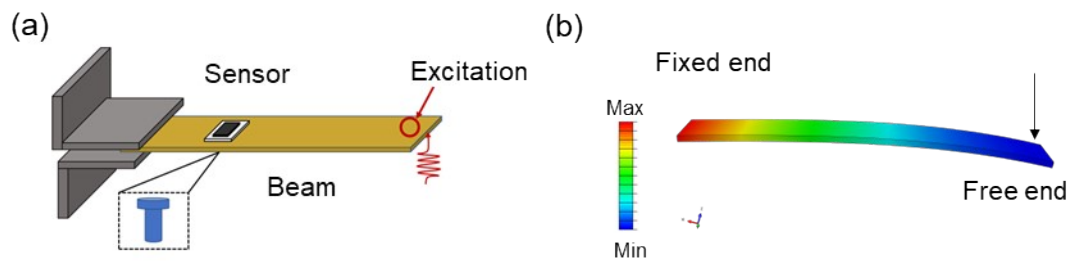


Figure S27. Schematic illustrations and FEA analysis of vibration generation and dynamic detection system

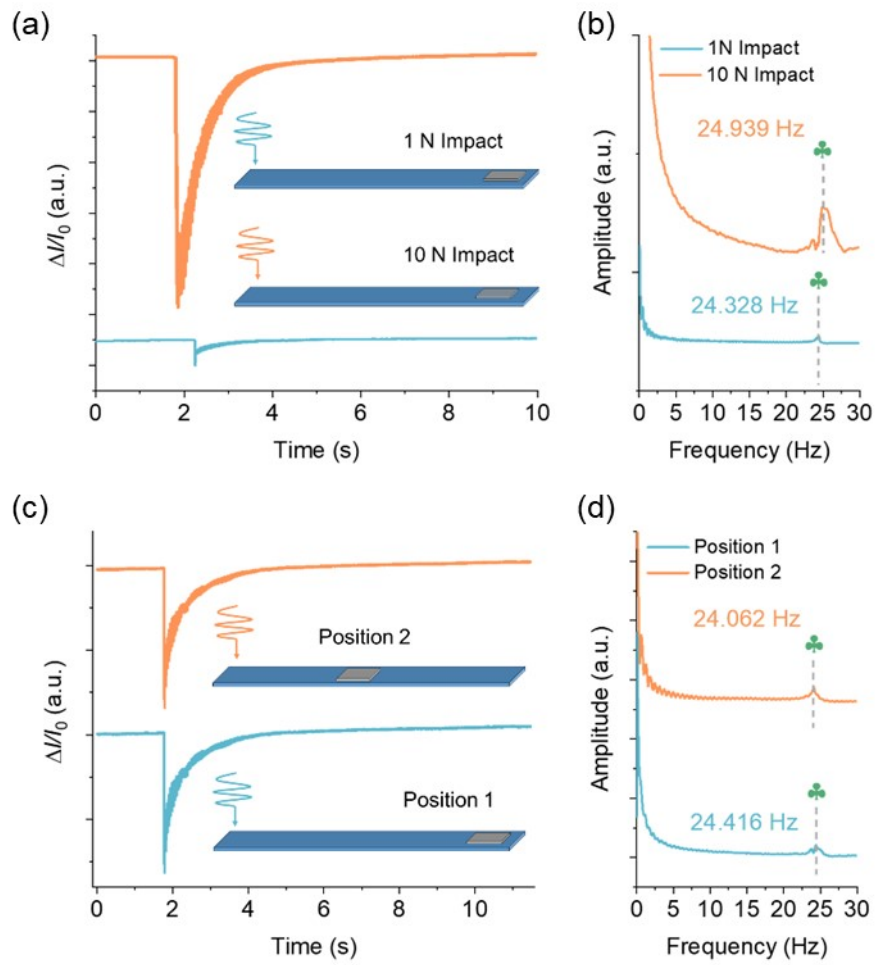


Figure S28. Time and frequency responses of the crack sensor attention in cantilever beam subjected to impact test. (a) time response of the sensor with different impact force, (b) corresponding frequency response. (c) time response of the sensor with impact at different position (d) corresponding frequency response

Figure S28 indicates that the time and frequency responses of the cantilever beam recorded by the crack vibration sensor. The impact response of the cantilever beam detected by the proposed vibration sensor was analogous. The sensor exhibited an excellent and stable response to the vibration. When the cantilever beam was subjected to impact, the signal response of the sensor increases and maintains a stable signal until the press was released. The natural frequency obtained by the crack sensor was approximately to 24 Hz compared with the result from the accelerometer 23.891 Hz. There is only 2% difference between the sensor and accelerometer.

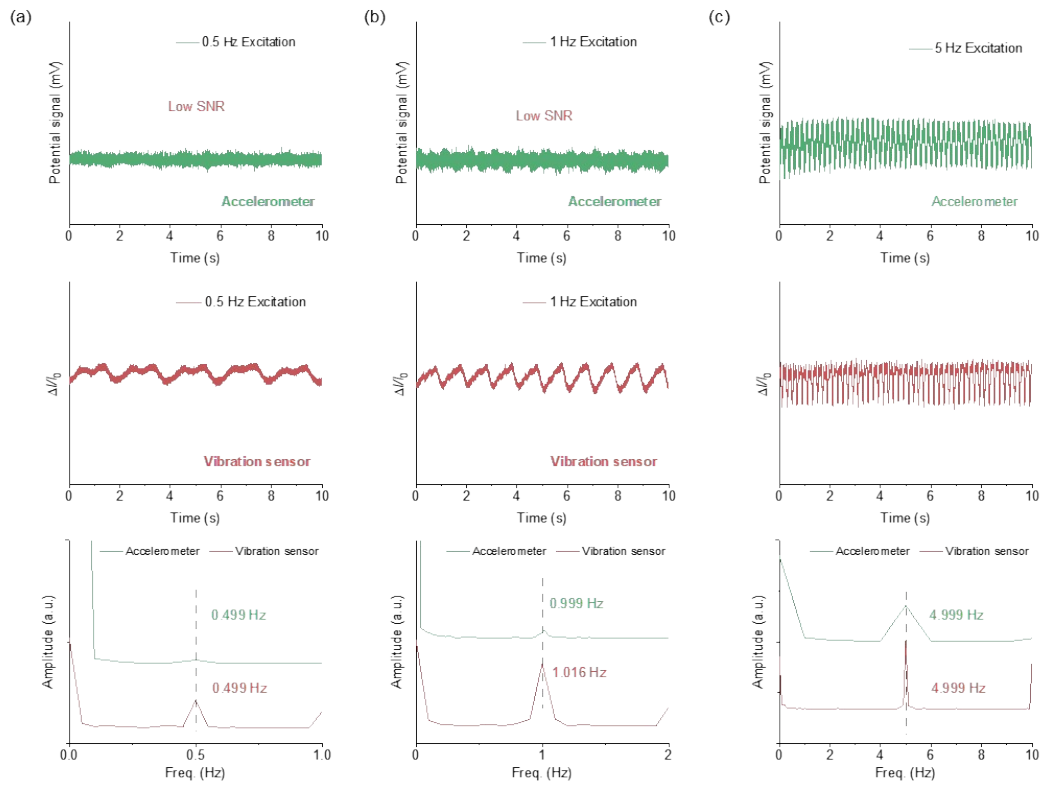


Figure S29. Time and frequency responses of the crack sensor subjected to base excitation with three different frequencies (a) 0.5 Hz, (b) 1 Hz and 5 Hz. Compare with commercial accelerometer.

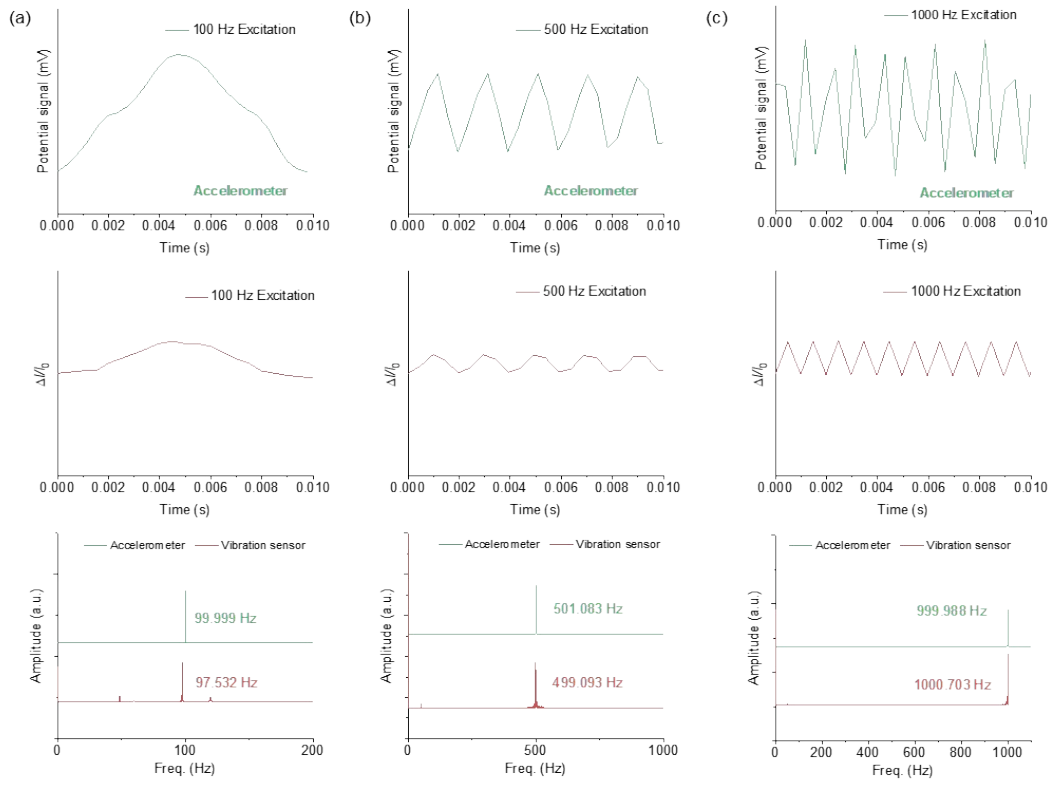


Figure S30. Time and frequency responses of the crack sensor subjected to base excitation with three different frequencies (a) 100 Hz, (b) 500 Hz and 1000 Hz. Compare with commercial accelerometer.

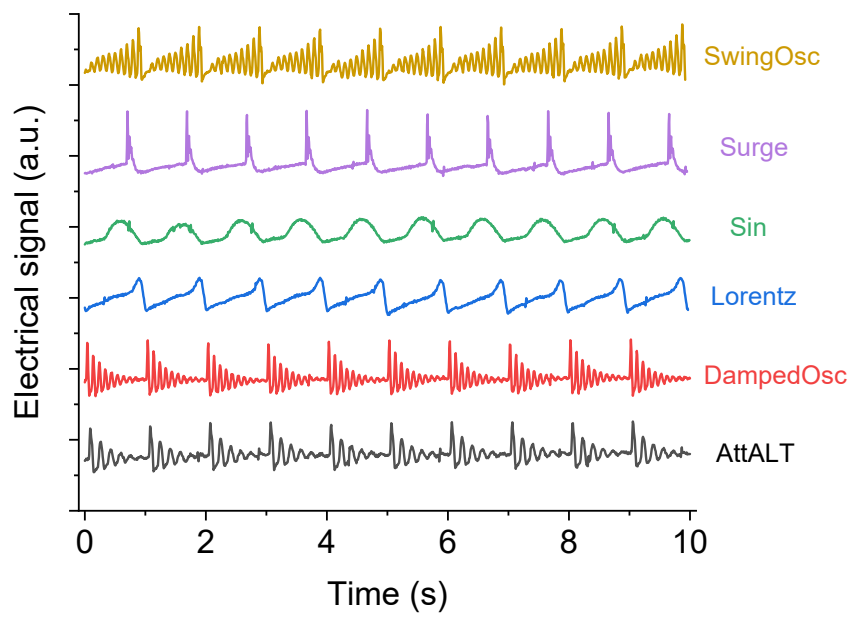


Figure S31. The recognition of the sensor to different input mechanical vibration waveforms.

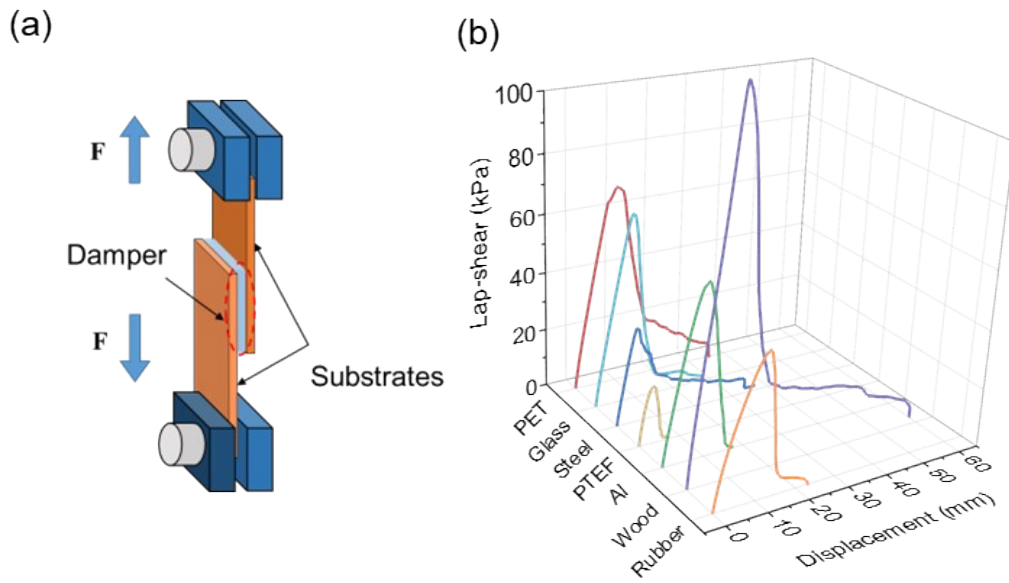


Figure S32. (a) Schematic diagram of the lap shear adhesive properties test. (b) Shear strength of gel damper to different materials.

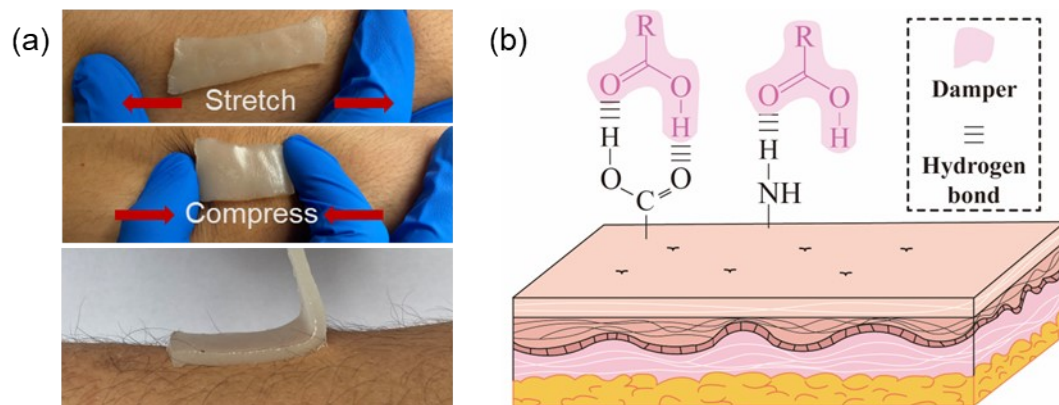


Figure S33. (a) Schematic diagram of the deformation and peeling of the damper attached to the skin surface. (b) Adhesive mechanism of gel damper to skin.

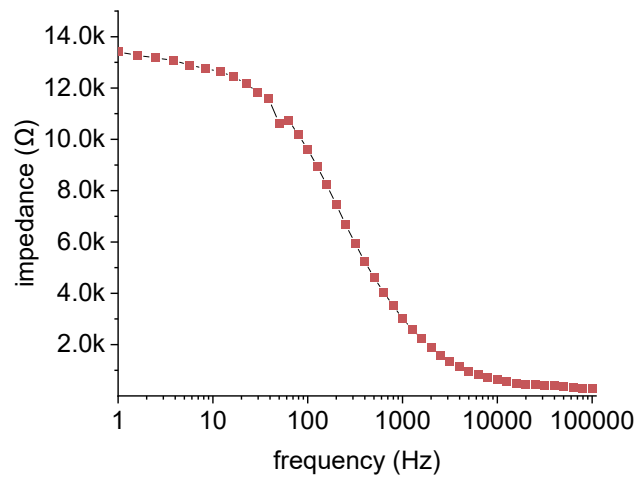


Figure S34. Contact impedance of damper electrode to skin.

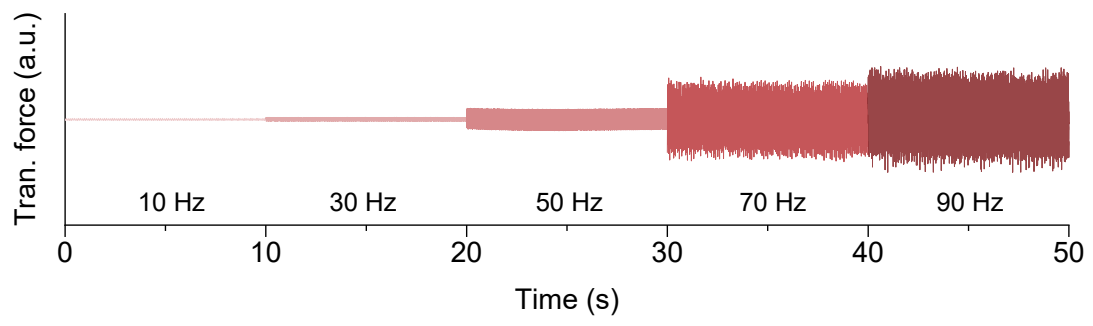


Figure S35. Equivalent circuit of a wireless sensor module.

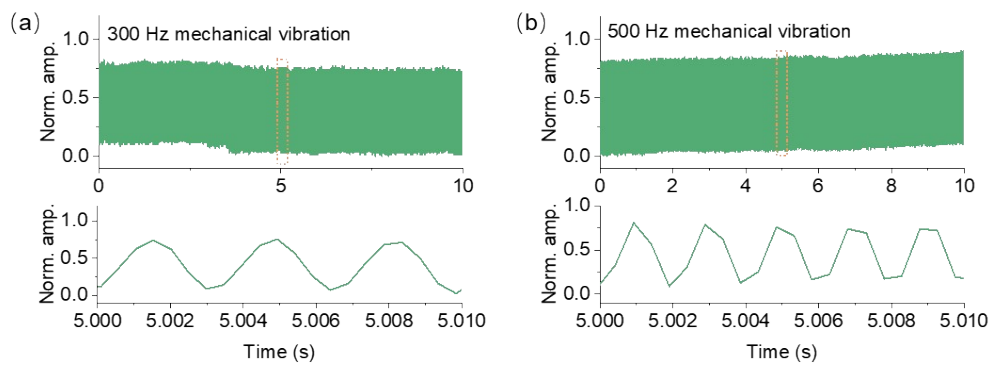


Figure S36. Normalized time-dependent vibrations waveforms of gel damper samples with applied (a) 300 and (b)500 Hz frequencies.

Table S1. Electromechanical performance of crack sensor and other sensing material.

Material	Sensitive (GF/S)	Sensing range (Strain/Pressure)	Detection limit (Strain/Pressure)	Response time (ms)	Durability Cycle	Reference
MXene@TPU	28510	800%	0.05%	3.4	3000000	This work
TPU/BNNS	35.7	160%	10%	-	5000	<i>Nat. Commun.</i> 2020 ⁴
CNT/PU/ecoflex	~33	400%	0.0075%	25	10 000	<i>Adv. Mater.</i> 2022 ⁵
TPU/Mxene/CNT	3.92×10^7	70%	0.001%	5	45000	<i>Adv. Mater.</i> 2021 ⁶
TPU/CB	8962.7	150%	0.5%	60	10000	<i>Nano-Micro Lett.</i> 2021 ⁷
PAM/laponite/H ₃ BO ₃	2.68	750%	5%	10	200	<i>Adv. Funct. Mater.</i> 2023 ⁸
TPU/CNT@MXene	363	100%	5%	-	200	<i>ACS Nano</i> 2021 ⁹
PDMS-Ag	18000	0.65%	0.2	258	7000	<i>Adv. Mater.</i> 2022 ¹⁰
PEDOT:PSS-PVA	2.67	300%	0.05%	-	2000	<i>Adv. Mater.</i> 2022 ¹¹
MXene-PVDF	1470	50%	5%	64	20000	<i>Nat. Commun.</i> 2022 ¹²
PEDOT:PSS islands	15.61	100%	1%	186	1000	<i>Matter</i> 2021 ¹³
PDES/CMFs ICs	3.71	1300%	0.5%	70	1000	<i>Adv. Funct. Mater.</i> 2022 ¹⁴
SWCNT/BBEs	2.18	100%	-	-	2500	<i>Nat. Commun.</i> 2023 ¹⁵
PAA-HEMA	1.1	400%	-	50	3000	<i>Adv. Mater.</i> 2023 ¹⁶
CNTs-EM	43842.1	2 Pa	20 kPa	40	10000	<i>Matter</i> 2022 ¹⁷
Mxene-CPM	990.4	1500 Pa	10 Pa	100	5000	<i>Matter</i> 2022 ¹⁸
BBP-MXene	1929.8	0.2 Pa	0.0063 Pa	50	10000	<i>Nat. Commun.</i> 2022 ¹⁹

Table S2. Vibration sensor performance and other sensing material.

Material	Response frequency	Sensing signal	Reference
MXene@TPU	0.1-1000 Hz	Tensile strain and vibration	This work
Cross-linked graphene aerogel	0.005–4000 Hz	Cycle compression and Vibration	<i>Small</i> 2022 ²⁰
CNT/PU/ecoflex	0-40 Hz	Tensile strain and vibration	<i>Adv. Mater.</i> 2022 ⁵
PVDF-TrFE	1Hz-1000 Hz	Dynamic pressure sensor	<i>Njp. Flexible electronics</i> ²¹
Al/PDMS-PVDF	5-600 Hz	Piezoelectric	<i>Nat. Commun.</i> 2022 ²²
Pt/PDMS	400 Hz	Crack-based sensor	<i>Proc. Natl. Acad. Sci.</i> 2020 ²³

Supplementary References

- 1 J. Gu, F. Li, Y. Zhu, D. Li, X. Liu, B. Wu, H. A. Wu, X. Fan, X. Ji, Y. Chen and J. Liang, *Adv. Mater.*, 2023, **35**, 1–12.
- 2 T. Zhou, C. Wu, Y. Wang, A. P. Tomsia, M. Li, E. Saiz, S. Fang, R. H. Baughman, L. Jiang and Q. Cheng, *Nat. Commun.*, 2020, **11**, 1–11.
- 3 D. Tan, X. Cao, J. Huang, Y. Peng, L. Zeng, Q. Guo, N. Sun, S. Bi, R. Ji and C. Jiang, *Adv. Sci.*, 2022, **9**, 2201443.
- 4 C. Tan, Z. Dong, Y. Li, H. Zhao, X. Huang, Z. Zhou, J. W. Jiang, Y. Z. Long, P. Jiang, T. Y. Zhang and B. Sun, *Nat. Commun.*, 2020, **11**, 1–10.
- 5 J. Gao, Y. Fan, Q. Zhang, L. Luo, X. Hu, Y. Li, J. Song, H. Jiang, X. Gao, L. Zheng, W. Zhao, Z. Wang, W. Ai, Y. Wei, Q. Lu, M. Xu, Y. Wang, W. Song, X. Wang and W. Huang, *Adv. Mater.*, 2022, **34**, 2107511.
- 6 Y. Zhao, W. Gao, K. Dai, S. Wang, Z. Yuan, J. Li, W. Zhai, G. Zheng, C. Pan, C. Liu and C. Shen, *Adv. Mater.*, 2021, **33**, 1–10.
- 7 X. Wang, X. Liu and D. W. Schubert, *Nano-Micro Lett.*, 2021, **13**, 1–19.
- 8 J. Zou, X. Jing, Z. Chen, S. J. Wang, X. S. Hu, P. Y. Feng and Y. J. Liu, *Adv. Funct. Mater.*, 2023, **33**, 1–12.
- 9 H. Wang, R. Zhou, D. Li, L. Zhang, G. Ren, L. Wang, J. Liu, D. Wang, Z. Tang, G. Lu, G. Sun, H. D. Yu and W. Huang, *ACS Nano*, 2021, **15**, 9690–9700.
- 10 L. Liu, S. Niu, J. Zhang, Z. Mu, J. Li, B. Li, X. Meng, C. Zhang, Y. Wang, T. Hou, Z. Han, S. Yang and L. Ren, *Adv. Mater.*, 2022, **34**, 1–7.
- 11 Z. Shen, Z. Zhang, N. Zhang, J. Li, P. Zhou, F. Hu, Y. Rong, B. Lu and G. Gu, *Adv. Mater.*, 2022, **34**, 1–8.
- 12 H. Yang, J. Li, X. Xiao, J. Wang, Y. Li, K. Li, Z. Li, H. Yang, Q. Wang, J. Yang, J. S. Ho, P. L. Yeh, K. Mouthaan, X. Wang, S. Shah and P. Y. Chen, *Nat. Commun.*, 2022, **13**, 5311.
- 13 H. Liu, S. Zhang, Z. Li, T. J. Lu, H. Lin, Y. Zhu, S. Ahadian, S. Emaminejad, M. R. Dokmeci, F. Xu and A. Khademhosseini, *Matter*, 2021, **4**, 2886–2901.
- 14 X. Sun, Y. Zhu, J. Zhu, K. Le, P. Servati and F. Jiang, *Adv. Funct. Mater.*, 2022, **32**, 1–10.
- 15 P. Xu, S. Wang, A. Lin, H. K. Min, Z. Zhou, W. Dou, Y. Sun, X. Huang, H. Tran and X. Liu, *Nat. Commun.*, 2023, **14**, In press.
- 16 J. Zhang, S. Shen, R. Lin, J. Huang, C. Pu, P. Chen, Q. Duan, X. You, C. Xu, B. Yan, X. Gao, Z. Shen, L. Cai, X. Qiu and H. Hou, *Adv. Mater.*, 2023, **35**, 1–18.
- 17 X. Wei, H. Li, W. Yue, S. Gao, Z. Chen, Y. Li and G. Shen, *Matter*, 2022, **5**, 1481–1501.

-
- 18 X. Shi, Y. Zhu, X. Fan, H. A. Wu, P. Wu, X. Ji, Y. Chen and J. Liang, *Matter*, 2022, **5**, 1547–1562.
- 19 X. Shi, X. Fan, Y. Zhu, Y. Liu, P. Wu, R. Jiang, B. Wu, H. A. Wu, H. Zheng, J. Wang, X. Ji, Y. Chen and J. Liang, *Nat. Commun.*, 2022, **13**, 1–10.
- 20 Z. Zeng, N. Wu, W. Yang, H. Xu, Y. Liao, C. Li, M. Luković, Y. Yang, S. Zhao, Z. Su and X. Lu, *Small*, 2022, **18**, 1–11.
- 21 H. Jin, Y. Kim, W. Youm, Y. Min, S. Seo, C. Lim, C. H. Hong, S. Kwon, G. Park, S. Park and H. J. Kim, *npj Flex. Electron.*, , DOI:10.1038/s41528-022-00216-1.
- 22 J. Zhang, H. Yao, J. Mo, S. Chen, Y. Xie, S. Ma, R. Chen, T. Luo, W. Ling, L. Qin, Z. Wang and W. Zhou, *Nat. Commun.*, 2022, **13**, 1–9.
- 23 H. Yao, W. Yang, W. Cheng, Y. J. Tan, H. H. See, S. Li, H. P. A. Ali, B. Z. H. Lim, Z. Liu and B. C. K. Tee, *Proc. Natl. Acad. Sci. U. S. A.*, 2020, **117**, 25352–25359.